Hindawi
Advances in Civil Engineering
Volume 2024, Article ID 6205478, 12 pages
https://doi.org/10.1155/2024/6205478

Research Article

Experiment Study on the Mechanical Behavior and Acoustic Emission Response of Thick and Hard Sandstone Roof in Xinjiang Mining Area

Dongdong Qin,[1] **Zechao Chang**,[2] **and Ze Xia**[2]

[1]*School of Mines, Shanxi Institute of Technology, Yangquan 045000, China*
[2]*School of Mines, China University of Mining and Technology, Xuzhou 221116, China*

Correspondence should be addressed to Zechao Chang; changzechao@cumt.edu.cn

Received 30 October 2023; Revised 31 December 2023; Accepted 11 January 2024; Published 24 January 2024

Academic Editor: Bang Yeon Lee

One of the primary threats to coal mine safety production is the sudden extensive fracturing and collapse of thick and hard roof strata. A range of uniaxial compression experiments with acoustic emission (AE) monitoring was performed for studying the mechanical properties and crack evolution of thick and hard roof sandstone specimens. AE temporal response analysis revealed that the damage process of thick and hard roof sandstone specimens exhibited distinct stages. Additionally, AE event localization indicated that microcracks within the thick and hard roof sandstone specimens propagated from the ends to the middle of the specimens during the loading process, eventually leading to severe failure. The *b*-value analysis demonstrated that during the early loading stage, the scale of internal microcracks within the thick and hard roof sandstone specimens gradually decreased with the optimization of the load-bearing structure. In the later loading stage, the scale of microcracks increased with the deterioration of the load-bearing structure. Furthermore, RA–AF analysis revealed that the specimens experienced combined tensile–shear failure, primarily dominated by tensile failure throughout. The AE characteristics observed during the deformation of thick and hard sandstone can provide references for the monitoring of roof stability and early warning of potential disasters in thick and hard sandstone conditions.

1. Introduction

The sudden large-scale breaking of hard roof is one of the main disasters that threaten the safety of coal mine production [1–4]. However, with the gradual advance of coal resources mining from shallow to deep space, mine production is more and more seriously affected by complex geological condition, such as high in-suit stress, high-geothermal temperatures, high-osmotic pressures, strong excavation disturbances, and so on. The elastic strain energy accumulated by its hard roof increases significantly, which means higher risk of typical dynamic disasters such as rock burst, coal, and gas outburst [5–8]. Rock damage is the development, expansion, aggregation, connection, and penetration of initial fractures in rocks [9, 10]. Consequently, it is important to investigate the crack development and damage evolution process of hard roof for stability monitoring, deformation control, and disaster early warning of surrounding rock mass in deep engineering.

Acoustic emission (AE) refers to the phenomenon where localized transient elastic waves are emitted due to the rapid release of strain energy [11–13]. Because AE is extremely sensible to the generation and propagation of fractures in materials and structures, AE technology finds extensive applications in areas such as material damage detection. Abbas et al. [14] used AE and ultrasonic pulses to analyze the progressive failure process of composite specimens (sandstone-shale-sandstone) under uniaxial stress, providing guidance for evaluating the deformation behavior of rock masses with different lithologies between layers. Zhang et al. [15] monitored coal specimens, concrete specimens, and concrete-confined coal specimens in uniaxial compression trials to investigate the evolution of AE energy releasing and the position of AE events. This research delved into the internal

microcracks in coal specimens throughout the loading process, examining their developmental stages and spatiotemporal distribution. Liu et al. [16] analyzed the AE characteristics of sandstone at different depths and pointed out that the initiation strength and damage strength of sandstone decrease exponentially with depth, and the elastic release rate increases exponentially with depth. Liu et al. [17] monitored the frequency spectrum and energy characteristics of AE signals resulting from coal fracture in uniaxial compression trials. They investigated the close correlation between these AE signals and coal–rock loading and deformation. Kong et al. [18] provided a qualitative explanation of the internal crack evolution process in coal specimens under loading conditions. They employed AE counting and cumulative counting evolution to analyze this process and proposed a coal specimen damage variable based on AE counting. Their work enabled a quantitative analysis of the evolution of damage in coal specimens.

Moreover, AE technology can reveal progressive internal damage evolution in coal rocks that is not visible to the naked eye by analyzing the energy distribution and nonlinear characteristics of AE waveforms [19], including parameters such as the *b*-value [20], moment tensor [21, 22], and other AE parameters [23]. Ohtsu [24] discussed the inherent relationship between rise angle (RA)–average frequency (AF) relationship to the microcrack rupture mechanism, and introduced a microcrack classification method based on AE. Building upon RA and AF parameter features observed in the uniaxial loading process of sandstone, Zheng et al. [25] noted that both tensile cracking and shear cracking coexist during the sandstone failure process, with shear cracking predominating. Additionally, by considering the statistical relation between AE signal amplitude and frequency, the AE *b*-value was incorporated into rock engineering field. It has since gained widespread use in assessing crack sizes during the damage progression of rock materials [21, 26–28]. Furthermore, Huang et al. [9], based on the evolution pattern of the rock *b*-value, divided the stress damage process into three stages: a fluctuation stage corresponding to fracture compaction, a stable stage indicative of steady crack development, and a declining stage representing unstable crack development. Dang et al. [29] found that the *b*-value decreased with increasing confining pressure, indicating that the energy released by specimen failure was higher at high-confining pressure.

This paper conducted uniaxial compression tests on sandstone specimens within thick and hard roof from a mine in Xinjiang. We analyzed the evolution laws of AE characteristics such as AE counting, AE energy, and AE event distribution in rock samples during uniaxial compression are analyzed, and discussed the damage mechanism of thick and hard roof sandstone samples in detail. Additionally, the AE *b*-value, the RA–AF relationship, and the spatial fractal dimension of AE events during the failure process are studied, which further reveals the microscopic fracture damage mechanism in these specimens. This study can serve as a beneficial reference for the stability monitoring, deformation control, and disaster early warning systems related to the surrounding rock mass in deep earth engineering projects.

2. Experimental Program

2.1. Sandstone Specimens. The sandstone specimens used in the experiments were obtained from the immediate roof of a thick and hard sandstone stratum in the 1,101 workface of a mine located in Xinjiang, China. The workface is approximately 450 m deep on average. According to the core drilling records, the thickness of the immediate roof (main roof), which is composed of fine sandstone, measures 7.5 m. For the purpose of reducing the variability in testing results due to specimen selection, the specimens used in the experiments were all taken from the same core drilling hole. After extraction, the sandstone specimens were sealed with plastic wrap and transported in foam-padded wooden crates to preserve their initial structure and moisture content. Following the guidelines of the International Society for Rock Mechanics (ISRM) for rock mechanics testing, the extracted sandstone specimens were processed into cylinders with a diameter (D) of 50 mm and a height (H) of 100 mm. The dimensional error of the sandstone specimens did not exceed 0.03 mm, the unevenness of the both end faces was within 0.05 mm, and the deviation of the end faces from the axis was not over 0.25°. Five specimens were prepared for the experiment. As these specimens were sourced from the field, all specimens underwent wave speed testing to ensure their standardization. Based on this testing, the three specimens exhibiting the most similar wave speed characteristics were selected and designated as S1, S2, and S3.

2.2. Experimental Methods. Figure 1(a) displays the major testing equipment and monitoring system. The uniaxial compression experiment on sandstone specimens was performed by electrohydraulic servo universal test machine. The test adopts the displacement loading at a speed of 0.2 mm/min. Simultaneously, an AE monitoring system was employed for monitoring AE events during compression. The AE system was configured with a capture threshold of 40 dB and a specimen frequency of 2 MHz. Six AE sensors were arranged on the sandstone specimen surface to simultaneously collect the sandstone specimen's AE signals in the course of loading. The AE sensors had a working frequency scope of 125–750 kHz, with a resonant frequency at 140 kHz. The AE sensor arrangement and the prepared specimens are shown as Figures 1(b) and 1(c), respectively.

2.3. Analysis Methods

2.3.1. b-Value. According to the statistical relation between AE signal amplitude and frequency, the AE *b*-value is introduced to assess the trend in the development of crack sizes during the specimen's failure process. The AE *b*-value can be determined using the Gutenberg–Richter relationship from seismology [20] as follows:

$$\lg N(M) = a - bM, \tag{1}$$

where M represents the statistical magnitude, which is typically approximated by dividing the AE amplitude by 20, i.e., $M = A_{\mathrm{dB}}/20$. N represents the cumulative frequency of AE

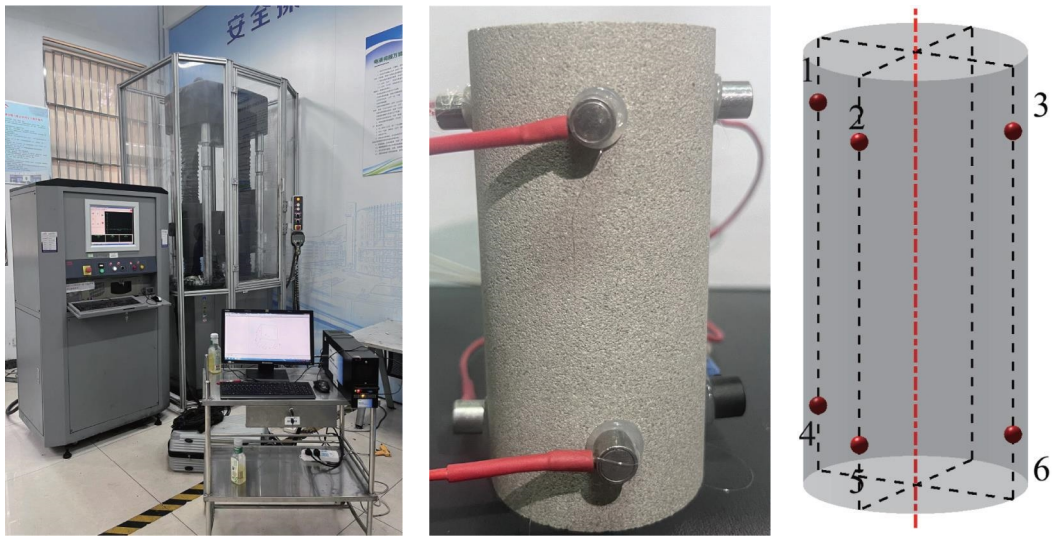

(a) (b) (c)

Figure 1: (a) Instruments and equipment, (b) prepared specimen, and (c) arrangement of AE sensors.

signals whose amplitudes are larger than or equal to M. a and b are constants, with b serving as the parameter that characterizes the scale of internal microcracks in rock during the damage process. Generally, high b-values reflect a greater share of small-scale microcrack events, suggesting that the internal damage primarily involves the development and propagation of small-scale cracks. This typically corresponds to a lower degree of damage in the sandstone specimen. Conversely, low b-values reflect a greater share of large-scale microcrack events, indicating that the material's internal structure involves the formation of finer and even macroscopic cracks, which typically corresponds to a higher degree of damage in the sandstone specimen. In order to understand the expansion of internal microcracks in the thick and hard roof sandstone specimens, the evolution of b-values throughout the entire uniaxial compression process was calculated based on Equation (1). To avoid significant errors caused by a small number of AE events within the sampling window, a 50-s event interval was used with a 10-s time step for sliding sampling. The amplitude interval was set at 5 dB.

2.3.2. RA–AF. Based on a large number of laboratory experiments and statistical analysis, AE signal has been extensively utilized for assessing fracture damage types in the sandstone specimens. This is because AE signals generated by tensile fractures typically have characteristics such as short waveforms, short rise times, and high frequencies, while AE signals produced by shear fractures tend to have long waveforms, long rise times, and lower frequencies. Therefore, signals of high AF and low RA are generally regarded as tensile fracture signals, whereas signals of low AF and high RA are associated with shear fracture signals [25, 30–32]. As shown in Equations (2) and (3), RA and AF are counted based on the parameters such as rising time, amplitude, ringing count, and duration within the AE signals [33] as follows:

$$\mathrm{RA} = \frac{\text{Rising time}}{\text{Amplitude}}, \tag{2}$$

$$\mathrm{AF} = \frac{\text{Ringing count}}{\text{Time interval}}, \tag{3}$$

where rising time represents the time interval in microseconds (μs) from when an AE event's signal first exceeds the threshold to while reaching its maximum amplitude; Amplitude represents the maximum of the AE signal's amplitude in volts (V); Ringing count represents the times when AE signal amplitude exceeds the threshold; Time interval represents the time interval in microseconds (μs) from when an AE event's signal first exceeds the threshold to the last time it reaches the threshold.

For this study, the AF/RA values of AE signals received by sensor 1# are used, and the maximum AF/RA, marked as k, was used as the crack classification threshold. AE events with AF/RA > k are identified as tensile fracture events, while those with AF–RA values below this threshold are defined as shear fracture events. It should be noted that before crack classification, the quantile function was used to filter out discrete data, and each sample had more than 98% of the total retained data, which can be considered representative.

2.3.3. AE Spatial Fractal. The AE spatial localization points can reflect the positions of internal microcracks in the specimen, and their evolution process exhibits fractal characteristics. To further investigate the damage mechanism, this study employs the box-dimension method to calculate the AE spatial fractal dimension (D_s). This method involves covering the specimen with three-dimensional cubes of side length r. If an AE localization is found within the cube, it is marked as nonempty; otherwise, it is marked as empty. The number of nonempty cubes $N(r)$ is counted, and as r approaches 0, D_s can be calculated as follows:

$$D_s = \lim_{r \to 0} \frac{\lg N(r)}{-\lg r}. \tag{4}$$

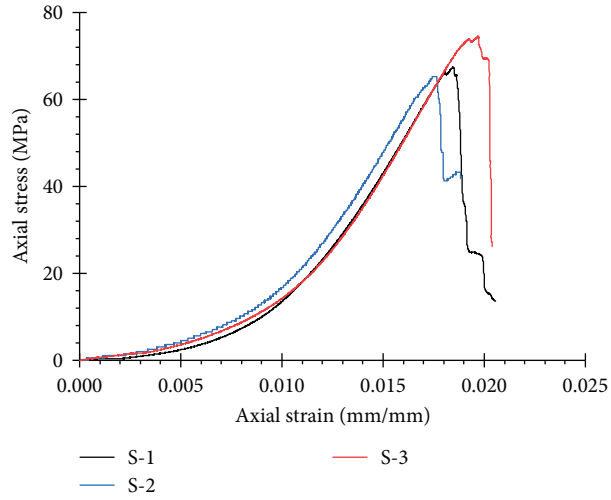

Figure 2: Stress–strain curves of specimens.

Table 1: Uniaxial compression experimental results.

Specimen no.	Peak stress (MPa)	Peak strain	Elastic modulus (GPa)
S1	67.39	0.0185	7.83
S2	35.16	0.0175	7.77
S3	74.42	0.0197	8.05
Average	68.99	0.0186	7.88

For natural fractals composed of discrete elements, the dimension of the box-dimension method can be defined as follows [34]:

$$N(r) = Cr^{-D_s}. \tag{5}$$

Taking the logarithm of both sides gives:

$$\lg N(r) = \lg C - D_s \lg r, \tag{6}$$

where C is the material constant.

3. Experiment Results and Analysis

3.1. Stress–Strain Behavior. Figure 2 displays the uniaxial compression stress–strain curves for the sandstone specimens, revealing a similarity in the stress–strain behavior of the specimens. As shown in Table 1, the average peak stress, peak strain and elastic modulus are 68.99, 0.0186, and 7.88 GPa, respectively.

During the uniaxial compression process, the combined response relationship between stress, strain, and AE activity in the thick and hard roof sandstone specimens during the damage process is illustrated in Figure 3, revealing that the development of strain–stress curves and AE responses in the thick and hard roof sandstone specimens during uniaxial compression is roughly separated into five phases.

(1) Fracture closure stage (OA, stress range 0%–20%): During this stage, the original cracks in the specimen experience closure due to compaction. The stress–strain curve exhibits an upward concave shape. Because of the randomness of natural defects inside the sandstone specimen, AE responses are relatively active but exhibit poor regularity. The AE count curve shows slow and irregular oscillations in growth, and the AE cumulative count curve increases gradually.

(2) Linear elastic stage (AB, stress range 20%–50%): The stress–strain curve approximately follows a linear upward trend. Although, a few microcracks may develop during this phase, along with the closure of original cracks, the level of AE response remains relatively stable or even decreases. The AE count curve remains relatively steady, and the AE cumulative count curve continues to increase linearly, yet with a lower speed than in Phase I.

(3) Stable crack development stage (BC, stress range 50%–80%): Microcracks inside the specimen steadily expand, leading to the irreversible deformation. The stress–strain curve exhibits nonlinear characteristics. AE responses gradually become more active, and the AE count curve shows a slight increase, while the AE cumulative count curve maintains a near-linear rise.

(4) Unstable crack development stage (CD, stress range 80%–100%): Internal cracks in the specimen rapidly expand, with numerous cracks intersecting, converging, and nucleating to form macroscopic main cracks.

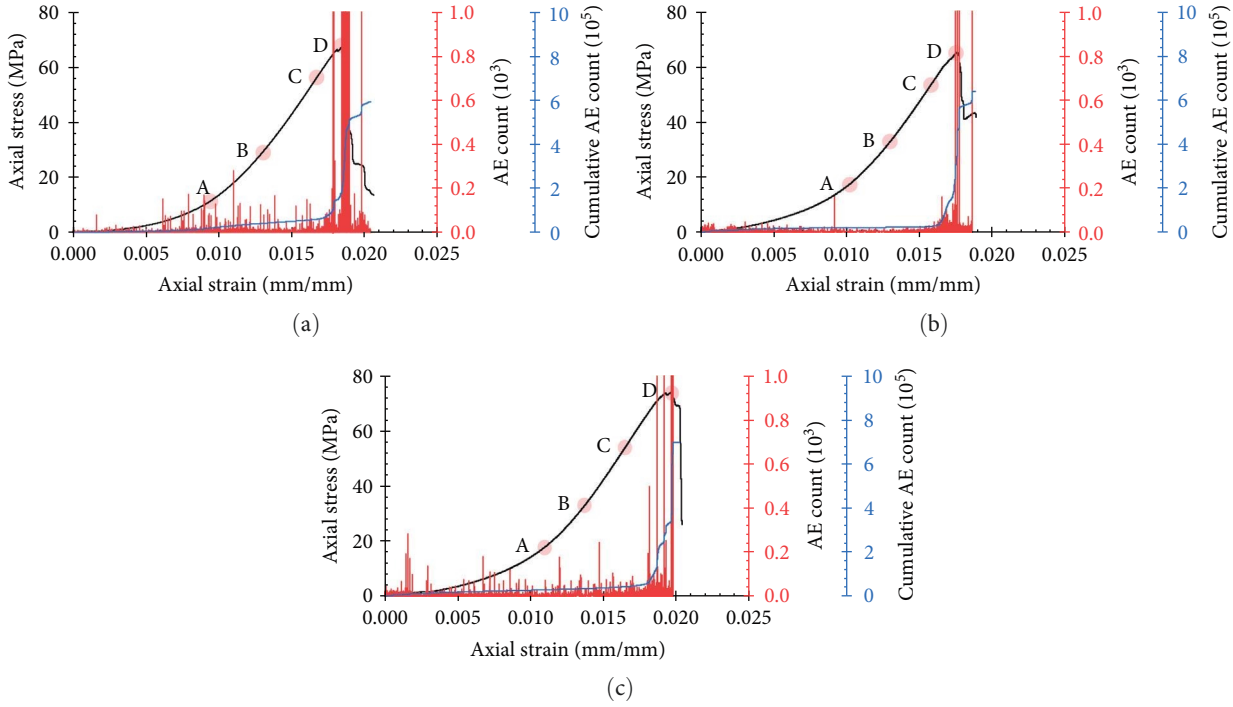

Figure 3: Stress–strain curves specimens: (a) S1, (b) S2, and (c) S3.

Extensive irreversible damage occurs within the specimen's internal structure, and the stress–strain curve becomes increasingly concave. AE counts increase rapidly, reaching a high level, and the AE cumulative count curve follows a parabolic growth pattern.

(5) Postpeak stage (D): Internal cracks in the specimen rapidly propagate to form the main failure surface, leading to a sudden drop in stress. Since, the specimen still retains some load-bearing capacity, multiple stress drops occur after the peak. AE activity is highly correlated with stress drops, resulting in a significant increase in AE counts to a high level, and the AE cumulative count curve exhibits a step-like increase.

3.2. AE Temporal Response. Figure 4 illustrates the stress, AE energy and accumulative count curves in the course of uniaxial compression of the sandstone specimen. Using the damage threshold as a reference, it can be observed that AE activity is highly correlated with the stress drops. Before significant stress drops occur, the AE energy curve fluctuates up and down at lower levels, and AE cumulative count grows slowly. After noticeable stress drops, AE energy sharply increases, and AE cumulative count exhibits astep-like rise. Furthermore, the AE responses of the specimen show distinct stage characteristics.

Using S2 as a typical specimen for analysis: (1) During early loading phases, AE signal is primarily induced by the closure and compaction of numerous preexisting cracks within the specimen. Hence, AE energy remains stable at a relatively low level during this stage, and AE cumulative count increases slowly. (2) Upon entering the elastic deformation stage, external loading is insufficient to initiate new microcracks. AE signal is primarily induced by further compaction and friction of the closed cracks within the specimen, resulting in AE energy remaining stable at a relatively low level. However, the rate of increase in AE cumulative count significantly decreases during this stage. (3) When entering the stage of stable crack expansion, the original microcracks inside the specimen begin to propagate, simultaneously initiating new microcracks. The AE energy curve experiences a substantial increase, and AE cumulative count starts to accelerate. (4) As the specimen enters the stage of unstable crack expansion, with further development of microcracks and communication with macroscopic cracks, the mechanical performance of the specimen significantly deteriorates. AE activity becomes highly active, AE signals significantly increase, and AE energy notably rises. The AE cumulative count follows an exponential-like sharp increase trend during this stage.

3.3. AE Spatial Response. To further investigate the failure process of the thick and hard roof sandstone specimens, AE event localization technology was employed to study the distribution of internal microcracks in the thick and hard roof sandstone specimens before reaching peak stress. Figure 5(a)–5(c) show the distribution of AE events during the fracture closure phase, linear elasticity phase, steady fracture development phase, and unsteady fracture development phase for specimens S1–S3, respectively. It is evident that the evolution of AE event localization in the uniaxial compression process of thick and hard roof sandstone specimens exhibits clear stage characteristics: (1) During the crack closure stage, AE events are relatively active, accumulating to

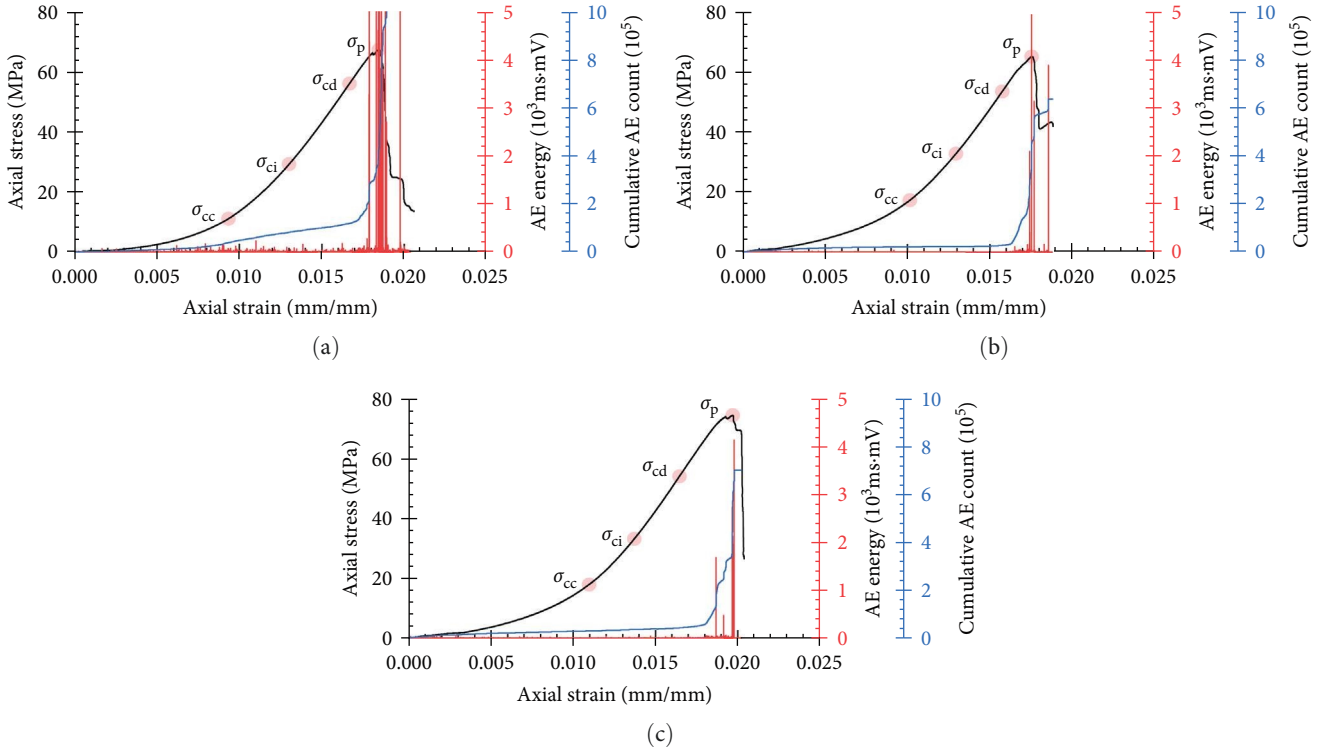

Figure 4: AE characteristics of specimens: (a) S1, (b) S2, and (c) S3.

varying degrees in the upper and lower parts of the specimen. (2) In the linear elasticity phase and steady fracture development phase, with further loading, AE events gradually propagate toward the middle of the specimen, and the accumulation area expands. This reflects the transition from localized damage to overall damage within the specimen. (3) In the unsteady fracture development phase, as the thick and hard roof sandstone specimen undergoes failure, significant AE events are generated and spread throughout the entire specimen.

4. Discussion

4.1. Analysis of AE b-Value. Figure 6 demonstrates the variation in *b*-values during the damage process of the thick and hard roof sandstone specimens, from which it is obvious that during the damage process of the sandstone specimen, the *b*-values exhibit fluctuations with increasing axial strain, but they show a relatively consistent overall evolution pattern. In the early loading stages, with the compaction and closure of the original pores, and the load-bearing structure of the specimen gradually optimizes, the scale of microcracks decreases, leading to an increase in *b*-values. In the later loading stages, as a large number of microcracks develop, potentially intersecting and inducing macroscopic fractures, the load-bearing structure of the specimen deteriorates, and the crack scale gradually increases, resulting in a decreasing trend in *b*-values.

4.2. Analysis of RA–AF. Figure 7 displays a density plot of the RA–AF relationship obtained through kernel density estimation. The blue scatters in the cloud diagram represents the maximum normalized data density (1.0) and the red scatters represents the minimum normalized data density (0.0). The blue area formed by the convergence of multiple blue scatters is defined as a high-density zone. The blue dotted line is the tension–shear crack classification line (slope *k*). It can be observed that most RA–AF data are distributed around the RA and AF axes and the high-density zone of RA–AF is mainly distributed above the tension–shear crack classification line. This phenomenon indicated that tensile and shear failure exist simultaneously during the uniaxial compression process but the tensile fractures being predominant.

To further qualitatively analyze the evolution of fractures in different damage stages during uniaxial compression, an analysis of shear and tensile crack evolution throughout the entire loading process of the thick and hard roof sandstone specimens is presented, as illustrated in Figure 8. It is evident that the evolution curves of shear and tensile cracks in the specimen exhibit distinct stage characteristics. Using S2 as a typical specimen for analysis: (1) In the stage of unstable crack expansion, both tensile and shear cracks rapidly increase, but the expansion speed of shear cracks is obviously lower than that of the tensile cracks. During this stage, the newly formed tensile cracks reach around 30% of the total tensile fractures, while shearing fractures account for only about 5% of the total shearing fractures. (2) As the specimen enters the stage of unstable crack expansion, with further development of microcracks and communication with macroscopic cracks, both tensile and shear cracks significantly increase. In this stage, the newly formed tensile cracks reach around 30% of the total

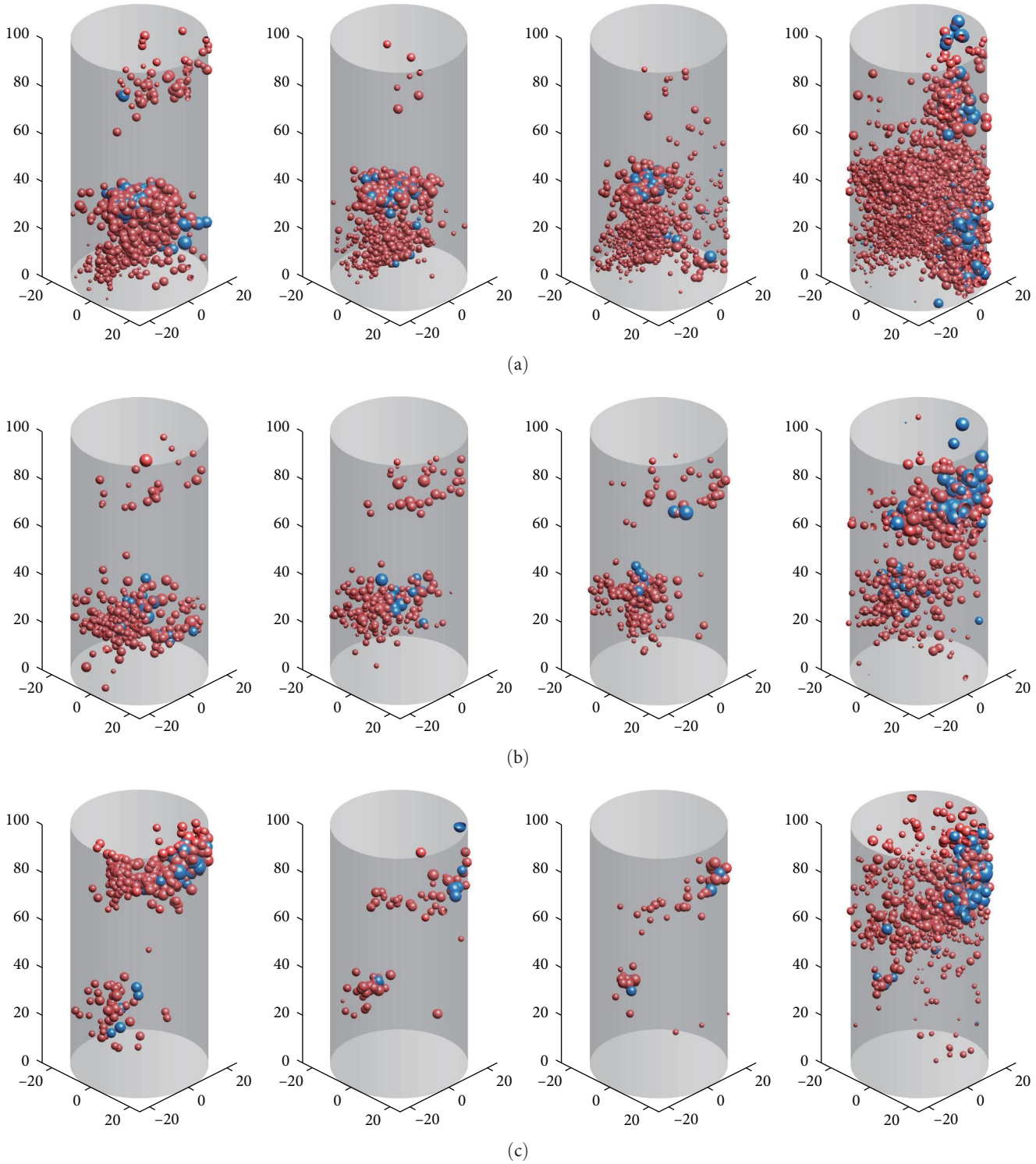

Figure 5: AE events evolution of specimens: (a) S1, (b) S2, and (c) S3 during different damage stages.

tensile fractures, while shearing fractures increase to about 25% of the total shearing fractures. (3) During the postpeak phase, both tensile and shearing cracks exhibit a substantial increase. During this stage, the newly formed tensile cracks reach around 40% of the total tensile fractures, while shearing fractures increase to about 70% of the total shearing fractures.

4.3. Analysis of AE Spatial Fractal. Taking into consideration the impact of scale invariance, the range of cube side lengths (r) is set between 1 and 10 mm. Figure 9(a)–9(c) displays the logarithmic plots of $N(r)$ versus $1/r$ for the thick and hard roof sandstone specimens, and linear fits are applied to the segments using the least-squares method. The slope of the

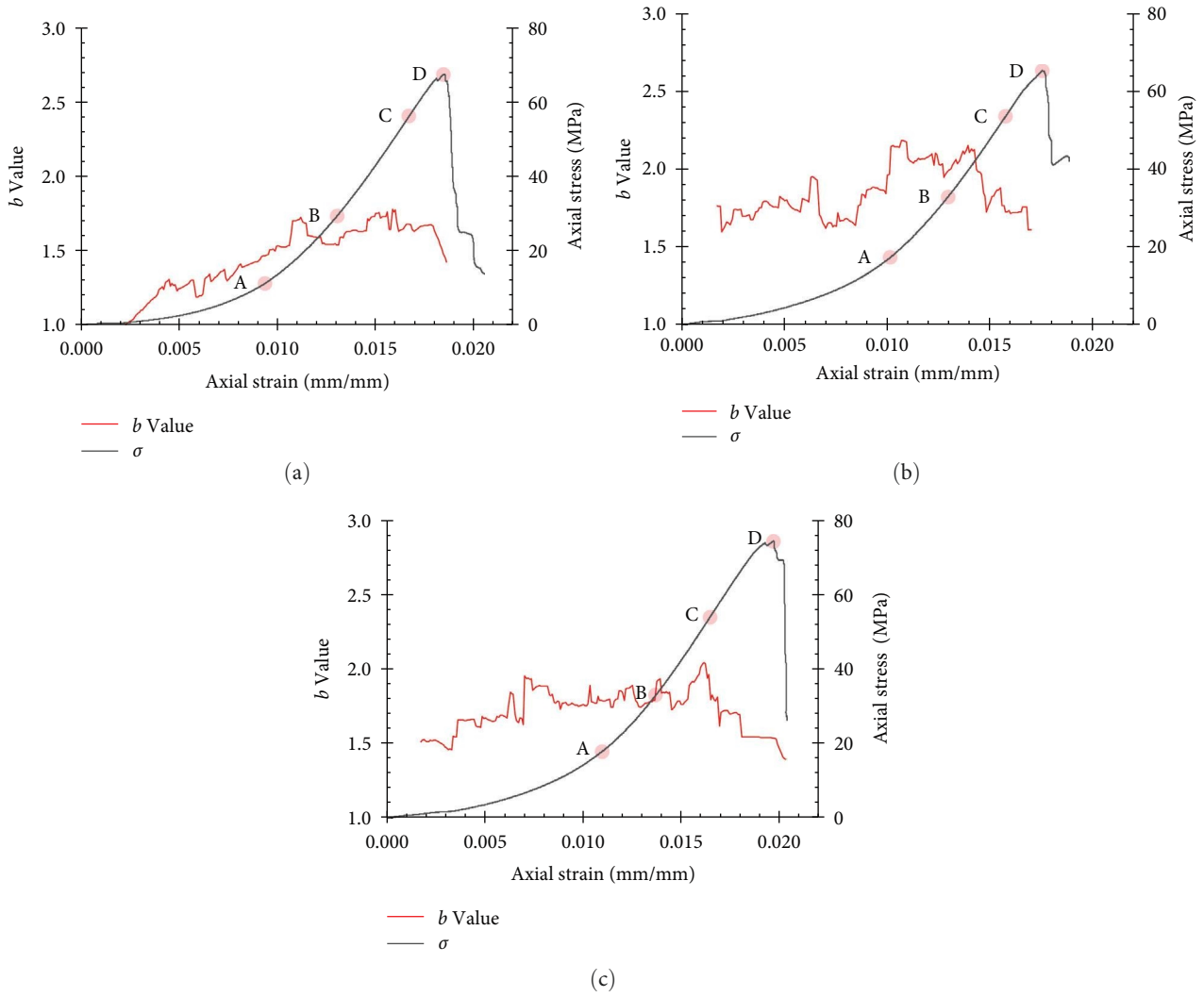

Figure 6: Variation of b-value of specimens: (a) S1, (b) S2, and (c) S3 during different damage stages.

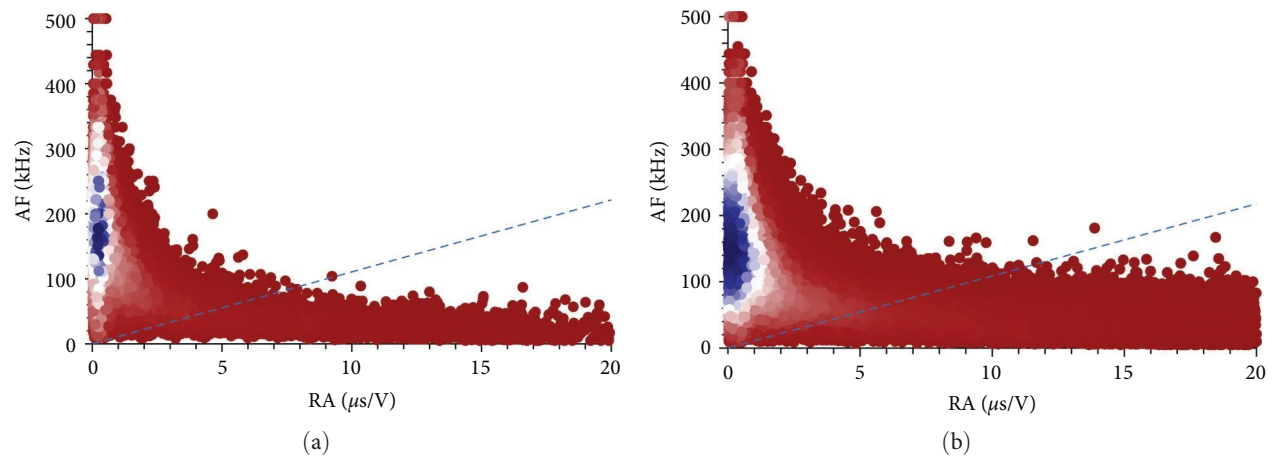

Figure 7: Continued.

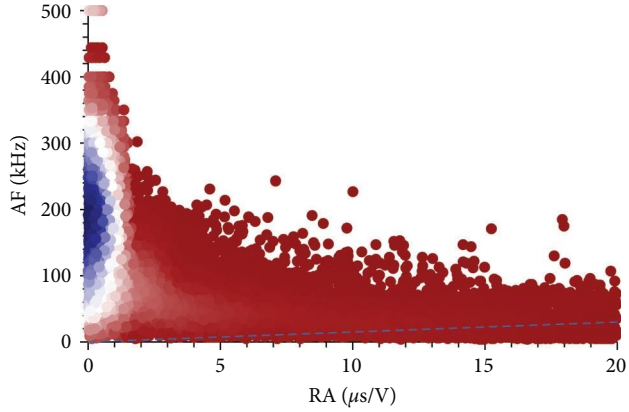

(c)

Figure 7: RA–AF of specimens: (a) S1, (b) S2, and (c) S3.

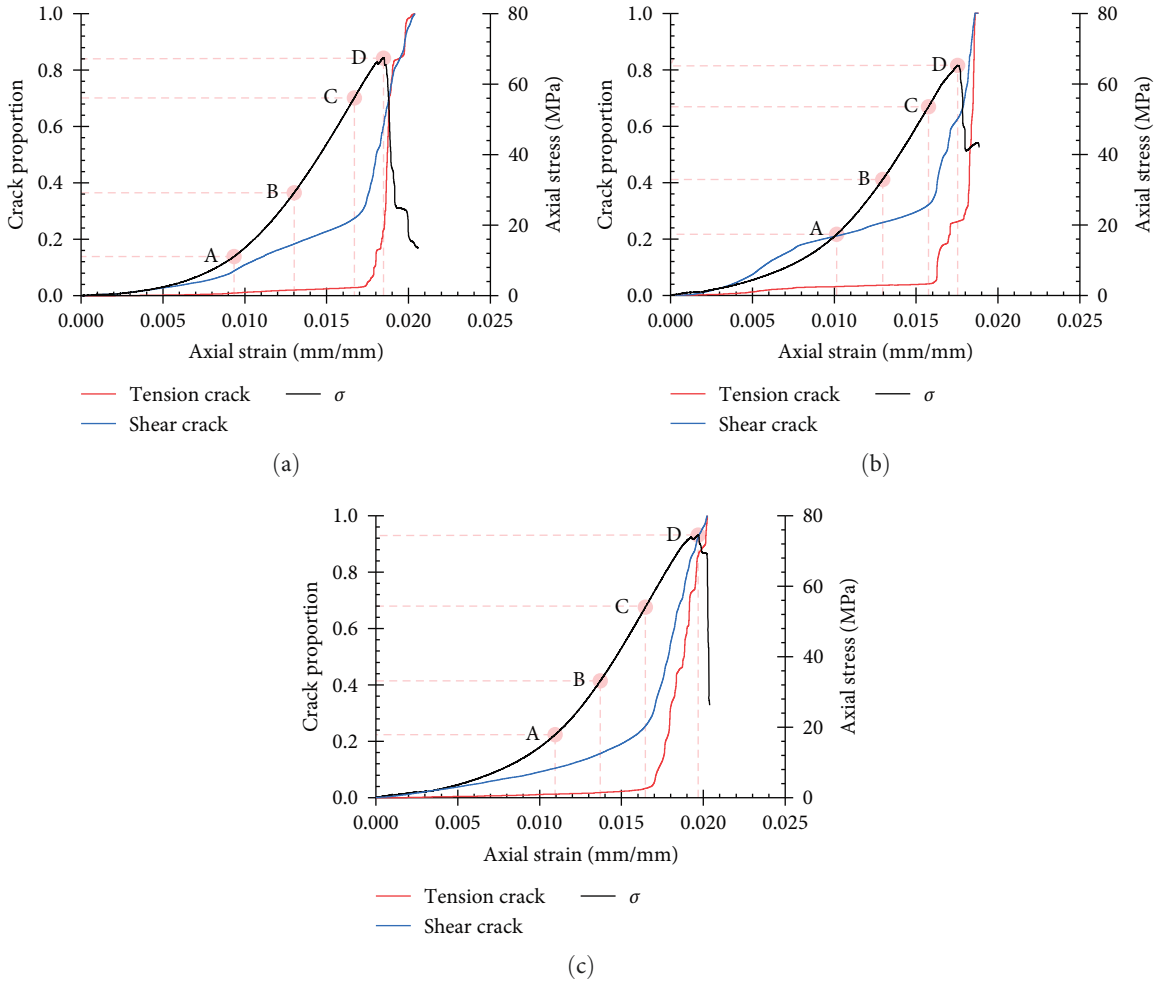

Figure 8: Shear and tension crack of specimens: (a) S1, (b) S2, and (c) S3.

fitted line corresponds to D_s. The statistical results of D_s for each thick and hard roof sandstone specimen, along with the goodness-of-fit R^2, are presented in Table 2. The correlation coefficients between the fitted data and the original data for each thick and hard roof sandstone specimen are all greater than 0.98, indicating that the AE spatial distribution exhibits fractal characteristics. Furthermore, the spatial fractal dimension is $D_s^1 > D_s^2 > D_s^3$ for the thick and hard roof sandstone specimens. Fractal dimension, as a measure of the disorder in nonlinear systems, implies an increase in the level of disorder in the system. Therefore, the degree of disorder in internal microcracks in the thick and hard roof sandstone

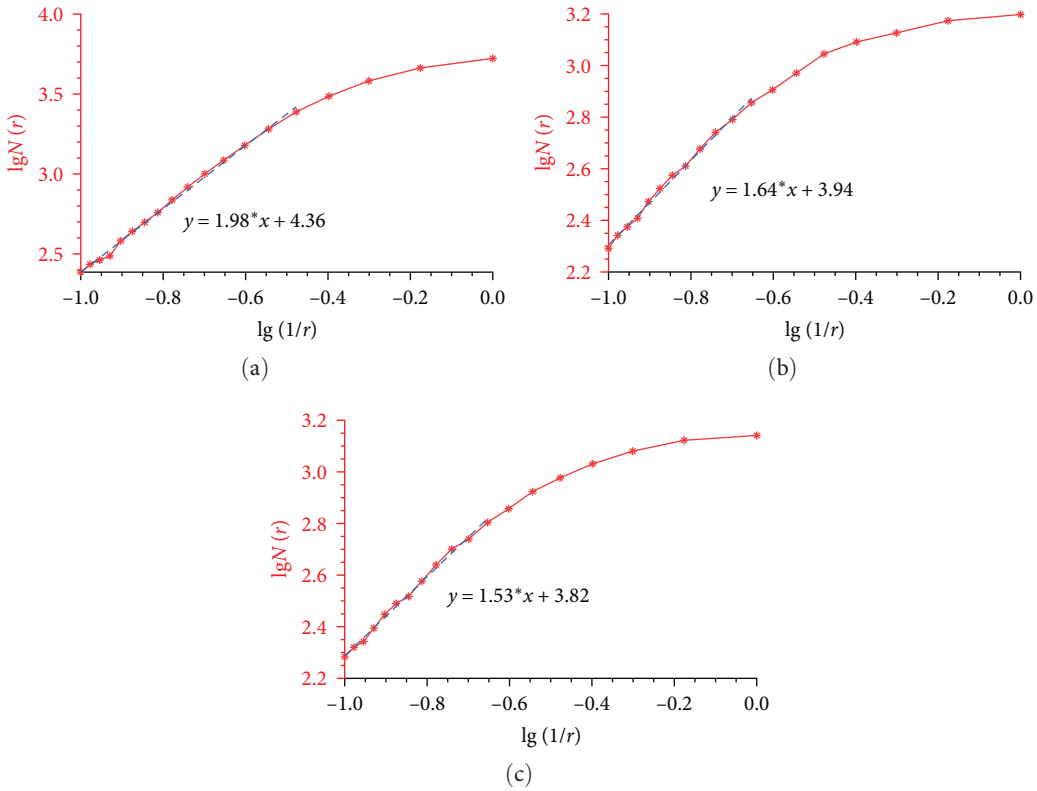

Figure 9: Relationship between lgN(r) and lg(1/r) of sandstone specimens: (a) S1, (b) S2, and (c) S3.

Table 2: Summary of the value of the fitting parameters.

Specimen no.	Fitting relationship	R^2	Fractal dimension
S1	$y = 1.98x + 4.36$	0.9973	1.98
S2	$y = 1.64x + 3.94$	0.9961	1.64
S3	$y = 1.53x + 3.82$	0.9962	1.53

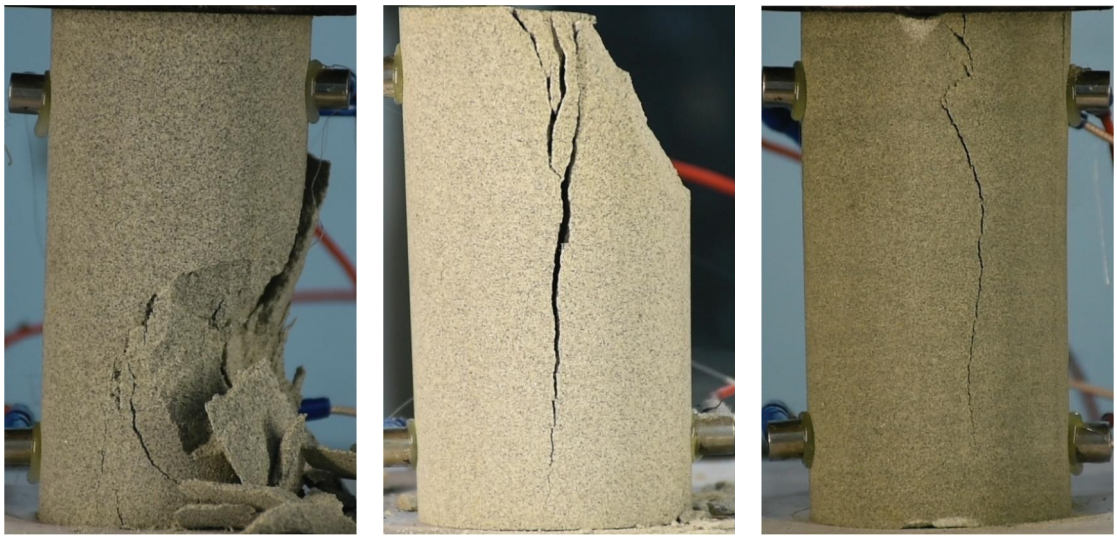

(a) (b) (c)

Figure 10: Failure pattern of specimens: (a) S1, (b) S2, and (c) S3.

specimens follows the order S1 > S2 > S3. This result is consistent with the experimental findings. As shown in Figure 10, by observing the degree of damage in the thick and hard roof sandstone specimens, it can be intuitively observed that: In S1, macroscopic cracks are concentrated in the middle and lower parts of the specimen, and the near-failure surface is segmented into relatively uniform fragments by the macroscopic cracks, indicating a higher degree of disorder in the crack system. In S2, macroscopic cracks develop from the upper part of the specimen to the lower part, resulting in a splitting-type failure of the specimen with a low degree of disorder in the crack system. In S3, the failure mode is similar to S2, but there are fewer secondary cracks near the fracture surface, leading to a further reduction in the disorder of the crack system.

5. Conclusion

During this paper, uniaxial compression experiments were carried out on sandstone specimens from a thick and hard roof in a Xinjiang mine. The analysis focused on the evolution of AE counts and AE event spatial distribution at different damage stages of the sandstone. Additionally, various indicators such as *b*-values, RA–AF ratios, and AE event spatial fractal dimensions were introduced to study the evolution of internal microcracks in the sandstone. The major findings are presented below:

(1) The thick and hard roof sandstone specimens exhibited low dispersion, and the stress–strain behaviour of specimens S1–S3 was similar. The average peak stress, peak strain, and elastic modulus were 68.99, 0.0186, and 7.88 GPa, respectively.

(2) AE time responses displayed significant stage-wise characteristics. Combined with the stress–strain curve features, the damage failure process of the sandstone specimens was separated into the crack compacted phase, linear elasticity phase, steady crack development phase, unsteady crack development phase, and postpeak phase.

(3) The spatiotemporal evolution of AE events vividly reflected the fracture extension process of sandstone specimens under compressive loads: early stage accumulation at the specimen ends, mid-stage expansion toward the middle, and late-stage distribution throughout the entire specimen.

(4) The *b*-value analysis demonstrated that during the early loading stage, the scale of internal microcracks within the thick and hard roof sandstone specimens gradually decreased. In the later loading stage, the scale of microcracks increased.

(5) RA–AF analysis revealed that the specimens experienced combined tensile–shear failure, primarily dominated by tensile failure. In the early loading stage, tensile cracks increases rapidly while shear cracks accumulate slowly. Then, both of tensile and shear cracks increase exponentially.

(6) AE event spatial fractal dimensions can be used as a measure of the crack disorder degree in the specimen.

Data Availability

Data supporting this research article are available on request.

Conflicts of Interest

The authors declare that they have no known competing financial interests or personal relationships that could have appeared to influence the work reported in this paper.

Acknowledgments

This research was funded by the National Natural Science Foundation of China (Grant No. 52104140) and Scientific and Technologial Innovation Programs of Higher Education Institutions in Shanxi (Grant No. 2021L580).

References

[1] M. Yu, J. Zuo, Y. Sun, C. Mi, and Z. Li, "Investigation on fracture models and ground pressure distribution of thick hard rock strata including weak interlayer," *International Journal of Mining Science and Technology*, vol. 32, no. 1, pp. 137–153, 2022.

[2] C.-P. Lu, G.-J. Liu, Y. Liu, N. Zhang, J.-H. Xue, and L. Zhang, "Microseismic multi-parameter characteristics of rockburst hazard induced by hard roof fall and high stress concentration," *International Journal of Rock Mechanics and Mining Sciences*, vol. 76, pp. 18–32, 2015.

[3] Y. Lu, T. Gong, B. Xia, B. Yu, and F. Huang, "Target stratum determination of surface hydraulic fracturing for far-field hard roof control in underground extra-thick coal extraction: a case study," *Rock Mechanics and Rock Engineering*, vol. 52, no. 8, pp. 2725–2740, 2019.

[4] Z. Tong, L. Changyou, K. Yetilmezsoy, Z. Baisheng, and Z. Shuai, "Fractural structure of thick hard roof stratum using long beam theory and numerical modeling," *Environmental Earth Sciences*, vol. 76, no. 21, pp. 1–13, 2017.

[5] G. Feng and P. Wang, "Simulation of recovery of upper remnant coal pillar while mining the ultra-close lower panel using longwall top coal caving," *International Journal of Mining Science and Technology*, vol. 30, no. 1, pp. 55–61, 2020.

[6] B. Huang, J. Liu, and Q. Zhang, "The reasonable breaking location of overhanging hard roof for directional hydraulic fracturing to control strong strata behaviors of gob-side entry," *International Journal of Rock Mechanics and Mining Sciences*, vol. 103, pp. 1–11, 2018.

[7] G. Wu, W. Yu, J. Zuo, and S. Du, "Experimental and theoretical investigation on mechanisms performance of the rock–coal–bolt (RCB) composite system," *International Journal of Mining Science and Technology*, vol. 30, no. 6, pp. 759–768, 2020.

[8] T. Zhang, L. Yu, H. Su, Q. Zhang, and S. Chai, "Experimental and numerical investigations on the tensile mechanical behavior of marbles containing dynamic damage," *International Journal of Mining Science and Technology*, vol. 32, no. 1, pp. 89–102, 2022.

[9] Z. Huang, Q. Gu, Y. Wu et al., "Effects of confining pressure on acoustic emission and failure characteristics of sandstone,"

International Journal of Mining Science and Technology, vol. 31, no. 5, pp. 963–974, 2021.

[10] F. Gao, S. Cao, K. Zhou, Y. Lin, and L. Zhu, "Damage characteristics and energy-dissipation mechanism of frozen-thawed sandstone subjected to loading," *Cold Regions Science and Technology*, vol. 169, Article ID 102920, 2020.

[11] J. Li, J. Zhao, H. C. Wang, K. Liu, and Q. B. Zhang, "Fracturing behaviours and AE signatures of anisotropic coal in dynamic Brazilian tests," *Engineering Fracture Mechanics*, vol. 252, Article ID 107817, 2021.

[12] X. Kong, E. Wang, X. He, D. Li, and Q. Liu, "Time-varying multifractal of acoustic emission about coal samples subjected to uniaxial compression," *Chaos, Solitons & Fractals*, vol. 103, pp. 571–577, 2017.

[13] J. Wang, J. Fu, W. Song, and Y. Zhang, "Mechanical properties, damage evolution, and constitutive model of rock-encased backfill under uniaxial compression," *Construction and Building Materials*, vol. 285, 2021.

[14] H. A. Abbas, Z. Mohamed, and S. A. Kudus, "Deformation behaviour, crack initiation and crack damage of weathered composite sandstone-shale by using the ultrasonic wave and the acoustic emission under uniaxial compressive stress," *International Journal of Rock Mechanics and Mining Sciences*, vol. 170, Article ID 105497, 2023.

[15] C. Zhang, Z. Jin, G. Feng, X. Song, G. Rui, and Z. Yujiang, "Double peaked stress–strain behavior and progressive failure mechanism of encased coal pillars under uniaxial compression," *Rock Mechanics and Rock Engineering*, vol. 53, no. 7, pp. 3253–3266, 2020.

[16] B. Liu, Y. Zhao, C. Zhang, J. Zhou, Y. Li, and Z. Sun, "Characteristic strength and acoustic emission properties of weakly cemented sandstone at different depths under uniaxial compression," *International Journal of Coal Science & Technology*, vol. 8, no. 6, pp. 1288–1301, 2021.

[17] S. Liu, X. Li, Z. Li, P. Chen, X. Yang, and Y. Liu, "Energy distribution and fractal characterization of acoustic emission (AE) during coal deformation and fracturing," *Measurement*, vol. 136, pp. 122–131, 2019.

[18] X. Kong, E. Wang, X. He, E. Zhao, and C. Zhao, "Mechanical characteristics and dynamic damage evolution mechanism of coal samples in compressive loading experiments," *Engineering Fracture Mechanics*, vol. 210, pp. 160–169, 2019.

[19] Q. Yao, C. Zheng, X. Shang, L. Yan, C. Shan, and W. Wang, "Evolution of mechanical and acoustic emission characteristics of coal samples under different immersion heights," *Natural Resources Research*, vol. 32, no. 5, pp. 2273–2288, 2023.

[20] L. Dong, L. Zhang, H. Liu, K. Du, and X. Liu, "Acoustic emission *b* Value characteristics of granite under true triaxial stress," *Mathematics*, vol. 10, no. 3, Article ID 451, 2022.

[21] I. S. Colombo, I. G. Main, and M. C. Forde, "Assessing damage of reinforced concrete beam using "*b*-value" analysis of acoustic emission signals," *Journal of Materials in Civil Engineering*, vol. 15, no. 3, pp. 280–286, 2003.

[22] X. Wang, P. Asem, C. Hu, and J. F. Labuz, "Microcracking in tensile fracture of a brittle rock," *Engineering Fracture Mechanics*, vol. 251, Article ID 107789, 2021.

[23] Z. Xia, Q. Yao, X. Li et al., "Acoustic emission characteristics and energy mechanism of CFRP-jacketed coal specimens under uniaxial compression," *Construction and Building Materials*, vol. 342, Article ID 127936, 2022.

[24] M. Ohtsu, "Quantitative AE techniques standardized for concrete structures," *Advanced Materials Research*, vol. 13-14, pp. 183–192, 2006.

[25] Q. Zheng, Y. Xu, H. Hu, J. Qian, Y. Ma, and X. Gao, "Quantitative damage, fracture mechanism and velocity structure tomography of sandstone under uniaxial load based on acoustic emission monitoring technology," *Construction and Building Materials*, vol. 272, Article ID 121911, 2021.

[26] C. H. Scholz, "The frequency–magnitude relation of microfracturing in rock and its relation to earthquakes," *Bulletin of the Seismological Society of America*, vol. 58, no. 1, pp. 399–415, 1968.

[27] M. Rao and K. Lakshmi, "Analysis of *b*-value and improved b-value of acoustic emissions accompanying rock fracture," *Current Science*, vol. 89, no. 9, pp. 1577–1582, 2005.

[28] R. V. Sagar and M. V. M. S. Rao, "An experimental study on loading rate effect on acoustic emission based *b*-values related to reinforced concrete fracture," *Construction and Building Materials*, vol. 70, pp. 460–472, 2014.

[29] Y. Dang, Z. Yang, and H. Zhu, "Study on failure mechanism of tight sandstone based on moment tensor inversion," *Heliyon*, vol. 9, no. 8, Article ID e19030, 2023.

[30] Q. Yao, T. Chen, C. Tang, M. Sedighi, S. Wang, and Q. Huang, "Influence of moisture on crack propagation in coal and its failure modes," *Engineering Geology*, vol. 258, Article ID 105156, 2019.

[31] G. Ma and Q. Du, "Structural health evaluation of the prestressed concrete using advanced acoustic emission (AE) parameters," *Construction and Building Materials*, vol. 250, Article ID 118860, 2020.

[32] C. Tang, Q. Yao, Q. Xu et al., "Mechanical failure modes and fractal characteristics of coal samples under repeated drying-saturation conditions," *Natural Resources Research*, vol. 30, no. 6, pp. 4439–4456, 2021.

[33] RILEM Technical Committee (Masayasu Ohtsu), "Recommendation of RILEM TC 212-ACD: acoustic emission and related NDE techniques for crack detection and damage evaluation in concrete*," *Materials and Structures*, vol. 43, no. 9, pp. 1187–1189, 2010.

[34] R. Zhang, F. Dai, M. Z. Gao, N. W. Xu, and C. P. Zhang, "Fractal analysis of acoustic emission during uniaxial and triaxial loading of rock," *International Journal of Rock Mechanics and Mining Sciences*, vol. 79, pp. 241–249, 2015.